RSC Advances

PAPER

View Article Online
View Journal | View Issue

Cite this: *RSC Adv.*, 2024, **14**, 1316

Removal of bromophenol blue from polluted water using a novel azo-functionalized magnetic nano-adsorbent†

Hadeel Saad,[ab] F. A. Nour El-Dien,[a] Nadia E. A. El-Gamel[a] and Ahmed S. Abo Dena *[cd]

Water pollution from organic dyes poses a serious danger to the environment. In the present work, we report a novel adsorbent (ADFS) based on azo-dye-functionalized superparamagnetic iron oxide nanoparticles (SPIONs) for the removal of the anionic dye bromophenol blue (BPB) from contaminated water. The fabricated SPIONs, azo dye, and ADFS adsorbent were characterized with FTIR and UV-vis absorption spectroscopy, ^{1}HNMR spectroscopy, mass spectrometry, SEM imaging, dynamic light scattering (DLS), zeta potential measurements, vibrating sample magnetometry, thermogravimetric analysis, differential thermal analysis, and X-ray diffraction analysis. DLS measurements showed a particle size of 46.1 and 176.5 nm for the SPIONs and the ADFS, respectively. The adsorbent exhibited an adsorption capacity of 7.43 mg g^{-1} and followed the pseudo-second-order kinetics model ($r^2 = 0.9981$). The ADFS could efficiently remove BPB from water after stirring for 120 minutes at room temperature and pH 2. The adsorption process was proved to occur *via* physisorption, as revealed by the Freundlich isotherm ($n = 1.82$ and $K_F = 11.5$). Thermodynamic studies implied that the adsorption is spontaneous ($-8.03 \leq \Delta G \leq -0.58$ kJ mol^{-1}) and enthalpy-driven might take place *via* van der Waals interactions and/or hydrogen bonding ($\Delta H = -82.19$ kJ mol^{-1} and $\Delta S = -0.24$ kJ mol^{-1} K^{-1}).

Received 23rd June 2023
Accepted 21st December 2023

DOI: 10.1039/d3ra04222g

rsc.li/rsc-advances

Introduction

Recently, the pollution of water resources has been grabbing the attention of researchers because it not only causes serious damage to the environment but also causes a serious economic loss that cannot be overlooked. Synthetic dyes belong to the most important water contaminants, and almost all of them are soluble in water, so their removal is very difficult. These dyes can be present in industrial effluents such as those from the food, paper, cosmetic, paint, textile, and leather industries. Accordingly, novel, efficient remediation and separation technologies are urgently needed for the removal of organic dyes from water so as to protect the water environment and human health.[1]

The common techniques reported in the literature for the removal of organic dyes from water include photocatalysis, oxidative degradation, coagulation, and other additional water-treatment approaches.[2] Unlike these approaches, adsorption-based water treatment methods exhibit some advantages, such as rapid removal, cost effectiveness, and easy manipulation. Bromophenol blue (BPB) is a well-known organic dye belonging to the triphenylmethane family. The IUPAC name of BPB is 2,6-dibromo-4-[3-(3,5-dibromo-4-hydroxyphenyl)-1,1-dioxo-2,1λ6-benzoxathiol-3-yl]phenol. It has been used as a pH indicator for a long time, and it is still being used in the textile, paint, leather, and paper industries. Other applications of BPB include using it as a tracking dye in electrophoresis and as a biological stain. The inhalation or contact of BPB may cause eye, skin and respiratory tract irritation. It may also cause foetal and reproductive effects. Liver, kidney and heart damage were reported in the case of prolonged inhalation to BPB.[3] In addition, the exposure to BPB can cause allergic reactions such as dermatitis, and respiratory problems. Moreover, oral administration of BPB can cause irritation of the GIT, nausea, vomiting, and diarrhoea. Accordingly, the direct discharge of dye-concentrated wastewater into the environment may cause a serious harm to the aquatic environment because they may increase the level of the total dissolved solids (TDS), chemical oxygen demand (COD), biochemical oxygen demand (BOD), and water turbidity.[4] That is why BPB may represent a serious danger to the environment due to the possibility of its leakage into the water from various sources. In this context, researchers

[a]*Chemistry Department, Faculty of Science, Cairo University, Giza, 12613, Egypt*
[b]*General Organization for Export and Import Control, Ramses Street, Cairo, Egypt*
[c]*Pharmaceutical Chemistry Department, National Organization for Drug Control and Research (NODCAR), Giza, Egypt. E-mail: ahmed_said5899@yahoo.com*
[d]*Faculty of Oral and Dental Medicine, Future University in Egypt (FUE), New Cairo, Egypt*

† Electronic supplementary information (ESI) available. See DOI: https://doi.org/10.1039/d3ra04222g

have been interested in finding new adsorbents for removing BPB from water in an efficient way.

In the last decade, many adsorptive approaches have been developed for the removal of BPB from contaminated water. For instance, biosorbents have been successfully applied for the removal of BPB, and they include black-soldier fly larvae,[5] haemoglobin,[6] and biopolymers.[7] In addition, magnetic hydrogels,[8] surfactant-coated selenium nanoparticles,[9] and matrix-dispersed polyethyleneimine-coated magnetic nanoparticles[10] were used as adsorbents for the removal of BPB from polluted water. Despite the effectiveness of the above adsorbents, most of them suffer from toxicity, high cost, unavailability, or complexity of the synthesis procedure.

The novelty of the present work is that it provides an approach to develop a new class of magnetic adsorbent materials that depend on superparamagnetic iron oxide nanoparticles (SPIONs) functionalized with a high-molecular-weight azo dye (AD). The proposed azo-dye-functionalized SPION (ADFS) adsorbent has the advantages of cost effectiveness, biocompatibility (since it uses biocompatible azo dye precursors), facile synthesis, and easy collection *via* the application of an external magnetic field. Moreover, the suggested ADFS adsorbent can be successfully applied for the removal of high concentrations of BPB from water at ambient temperature. The proposed ADFS adsorbent was fully characterized, and adsorption experiments were carried out so as to study adsorption isotherms, adsorption kinetics, and adsorption thermodynamics.

Materials and methods

Materials

Bromophenol blue was obtained from Carlo Erba Reagents (Barcelona, Spain). For the synthesis of the AD, *tert*-butyl-[2-(3,5-dihydroxyphenyl)-2-hydroxyethyl]azanium sulphate (TBDA sulphate, molar mass 548.65 g mol^{-1}, Borg Pharmaceutical Industries, Borg El-Arab, Alexandria, Egypt), aniline (Al-Alamia for Chemical Industries, Egypt), sodium carbonate (ADWIC, Egypt) and sodium nitrite (SDFCL, India) were used. Ferric chloride hexahydrate, $FeCl_3 \cdot 6H_2O$ (Daejung Chemicals and Metals, South Korea), anhydrous sodium acetate (ADWIC, Egypt) and ethylene glycol (Honeywell International Inc., USA) were used to synthesize the SPIONs. Hydrochloric acid was purchased from Alpha Chemika (India) and ethyl alcohol was obtained from the International Company for Medical Industries (Egypt). All chemical reagents were of analytical grade and were used as received without any further purification. A BPB stock solution (1000 mg L^{-1}) was prepared by dissolving 50 mg of BPB in 50 mL of double distilled water. Working BPB solutions (10–100 mg L^{-1}) were prepared by diluting a stock BPB solution (1000 mg L^{-1}) with distilled water shortly before each experiment.

Instruments

All absorbance measurements and spectral scans were carried out with the aid of a SPECORD 250 PLUS Analytikjena Spectrophotometer (Germany) with a 1 cm quartz cell. Field-emission scanning electron microscopy (FE-SEM; VEGA3 TESCAN, Czech Republic) and high-resolution transmission electron microscopy (HRTEM; JEOL JEM-2100, Japan) were used to study particle size, shape, and surface morphology. Fourier transform infrared spectra (FTIR) were recorded on a Nicolet 6700 ATR-FTIR spectrometer (Thermo Scientific, Germany). Particle size and zeta potential (ZP) of plain/uncoated SPIONs and the ADFS were determined by a Malvern Panalytical instrument (UK). A vibrating sample magnetometer (VSM, Lakeshore, Model 7410) was used to measure the magnetic properties of the synthesized nanomaterials. X-ray diffraction (XRD) spectra (Discover-D8, Bruker, USA) were used to unravel the crystal structure of the synthesized nanoparticles. ^{1}H NMR spectra were recorded with a Varian 300 MHz NMR spectrometer (Germany) with deuterated DMSO as a solvent. The pH measurements were carried out using a JENCO 6173 pH meter. The mass spectrum of the AD was recorded using a Q 1000 EX LC-MS Shimadzu (Japan).

Preparation of SPIONs

The SPIONs were prepared *via* a solvothermal method, described elsewhere, using ethylene glycol as a solvent.[11,12] In a typical synthesis, $FeCl_3 \cdot 6H_2O$ (2 g) and anhydrous sodium acetate (6 g) were dissolved in ethylene glycol (65 mL) under stirring. A homogeneous yellow solution was obtained. It was then transferred to a Teflon-lined stainless-steel solvothermal reactor and incubated at 200 °C in the oven (Heraeus, Thermo Electron Corporation, Germany) for 12 h. Thereafter, the solvothermal reactor was allowed to cool down to room temperature. The black magnetite nanoparticles were washed several times with distilled water and ethanol to remove the unreacted reagents, and then dried in a vacuum oven at 30 °C overnight.

Preparation of ADFS

The ADFS was synthesized *via* a diazo coupling reaction according to the procedure described elsewhere with minor modifications (Fig. 1).[13] First, 2.0 mL of aniline (22 mmol), 15 mL of double distilled water, and 5.0 mL of concentrated HCl were added to 1.0 g of SPIONs at 4 °C. After stirring for 20 min, a solution of sodium nitrite (2.0 g, 29 mmol) was dropped onto the above mixture at 4 °C with constant stirring. Then the resulting acidic solution was treated with 0.5 M sodium carbonate solution (50 mL) to neutralize the acidity of the mixture, followed by the dropwise addition of a solution of TBDA sulphate (1.0 g, 3.0 mmol) in 5.0 mL of double-distilled water with constant stirring. Finally, the mixture was stirred for 12 h at ambient temperature. The obtained reddish-brown precipitate (ADFS) was collected from the solution by using a powerful permanent magnet, washed several times with distilled water, and then air dried overnight at room temperature.

Adsorption experiments

Batch adsorption experiments are usually used to treat small volumes of the adsorbate in the laboratory. During batch

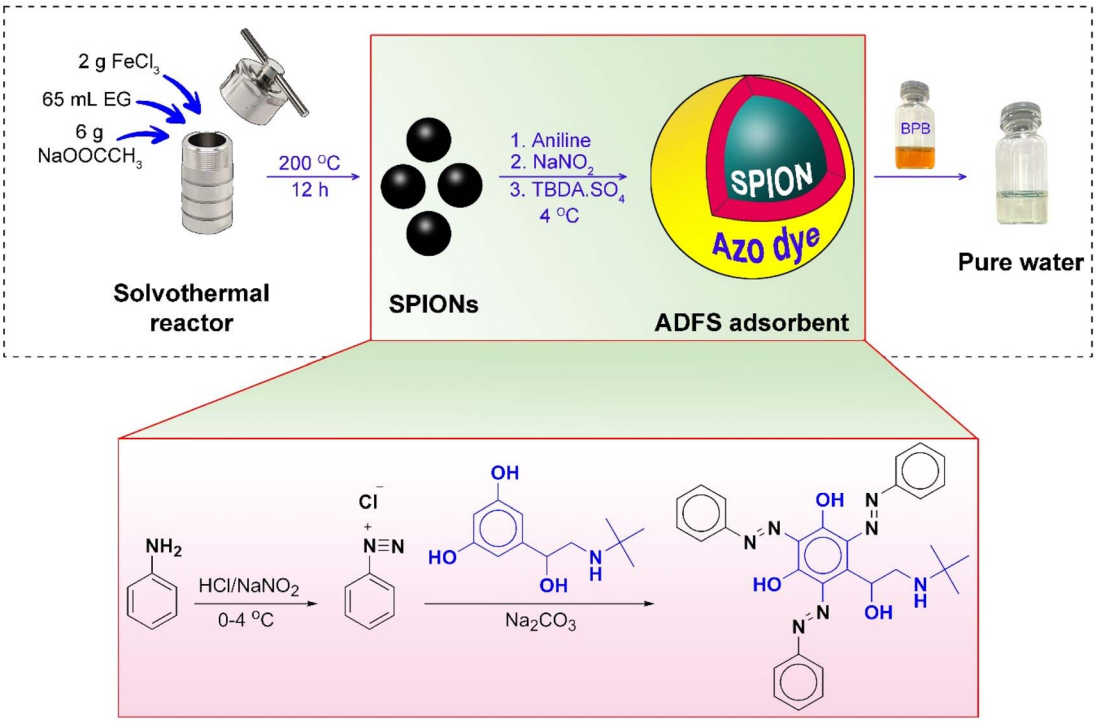

Fig. 1 An illustration showing the solvothermal preparation of SPIONs, synthesis of the aniline-based diazonium salt followed by coupling with TBDA sulphate, coating of SPIONs with AD, and water purification using the resultant ADFS adsorbent.

experiments, different parameters such as pH, contact time, initial BPB concentration, adsorbent dose, and temperature were investigated.[14] All experiments were conducted by mixing 20 mg of ADFS and 10 mL of BPB solution in tightly sealed 50 mL Erlenmeyer flasks at 400 rpm in a temperature-controlled shaker (Clifton, UK). The solution pH (pH 2–9) was adjusted using buffer solutions. After reaching equilibrium, the adsorbent was separated with a strong magnet. The remaining supernatant was filtered, and the uptake of BPB was assessed at 436 nm.

The effect of contact time on the adsorption of BPB on ADFS was investigated over time intervals from 10 min to 240 min at pH 2.0, an initial BPB concentration of 20 mg L^{-1}, an adsorbent dose of 20 mg, and room temperature (303 K). Moreover, the influence of the initial BPB concentration on the adsorption capacities of ADFS was studied using a BPB concentration range of 10–100 mg L^{-1}, pH 2.0, an incubation period of 120 min at room temperature (303 K), and 20 mg of ADFS. Furthermore, to determine the effect of the adsorbent dose on the adsorption of BPB from aqueous solutions, adsorption experiments were carried out by varying the amount of ADFS from 20 to 250 mg while keeping the remaining parameters unchanged. Finally, the effect of temperature on the removal efficiency of ADFS was studied over the temperature range of 303–333 K, using an adsorbent dose of 20 mg, a pH of 2.0, and a contact time of 120 min.

The percent removal (%R) and equilibrium adsorption capacity (q_e) of BPB were calculated using eqn (1) and (2):

$$\%R = \frac{(C_0 - C_e)}{C_0} \times 100 \quad (1)$$

$$q_e = \frac{(C_0 - C_e)}{m} \times V \quad (2)$$

where C_0 and C_e are the initial and final concentrations of BPB in mg L^{-1}, respectively, q_e is the adsorption capacity in mg g^{-1}, V is the solution volume in liters, and m is the adsorbent mass in grams.

Adsorption kinetics

Pseudo-first-order (PFO, eqn (3)), pseudo-second-order (PSO, eqn (4)), and intra-particle diffusion (IPD, eqn (5)) kinetic models were used to study the adsorbate–adsorbent interactions.[15–17]

$$\log(q_e - q_t) = \log q_e - (k_1/2.303)t \quad (3)$$

$$\frac{t}{q_t} = \frac{1}{k_2 q_e^2} + \frac{t}{q_e} \quad (4)$$

$$q_t = k_{id} t^{1/2} + I \quad (5)$$

where q_t (mg g^{-1}) is the adsorption capacity of BPB at time t, k_1 is the PFO rate constant of adsorption (L min^{-1}), t (min) is the contact time, k_2 (g mg^{-1} min^{-1}) is the PSO rate constant, k_{id} (mg g^{-1} $min^{-1/2}$) is the IPD rate constant, and I (mol g^{-1}) is a constant proportional to the boundary layer thickness.

Adsorption isotherms

Freundlich, Langmuir and Temkin isotherms. In the present study, the Langmuir (eqn (6)), Freundlich (nonlinear form, eqn

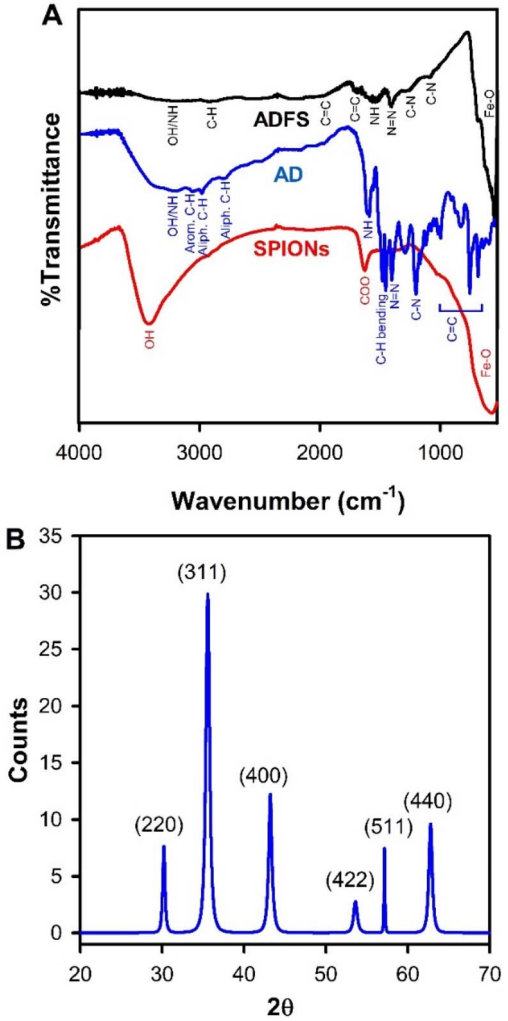

Fig. 2 (A) FTIR spectra of SPIONs, AD, and ADFS over the spectral range 4000–400 cm^{-1}. (B) XRD diffractogram of SPIONs depicting the X-ray diffraction planes.

(7); linear form, eqn (8)); and Temkin (eqn (9)) isotherm models were applied to describe the equilibrium between the adsorbed BPB on the surface of ADFS and the remaining BPB in the solution.[18,19]

$$\frac{C_e}{q_e} = \frac{1}{q_{max} b} + \frac{1}{q_{max}} C_e \quad (6)$$

$$q_e = K_F C^{1/n} \quad (7)$$

$$\log\ q_e = \log K_F + \frac{1}{n} \log C_e \quad (8)$$

$$q_e = \frac{RT}{b_T} \ln A_T + \frac{RT}{b_T} \ln C_e \quad (9)$$

where q_{max} (mg g^{-1}) is the maximum monolayer adsorption capacity, b (L mg^{-1}) is the Langmuir's constant related to the heat of adsorption, and K_F [(mg g^{-1})(mg L^{-1})^n] and n are the Freundlich isotherm constants related to the adsorption capacity and adsorption intensity, which describe the heterogeneity of the adsorbent surface, respectively; R is the universal gas constant (8.314 J K^{-1} mol^{-1}); T is the absolute temperature (K); $B = \frac{RT}{b_T}$ is a constant related to the heat of adsorption and indicates the adsorption potential of the adsorbent (J mol^{-1}); b_T is the Temkin isotherm constant; and A_T (L g^{-1}) is the Temkin equilibrium binding constant.[20,21]

Scatchard and Hill plots. Scatchard's and Hill's isotherms were used to study the nature of the binding sites. The Scatchard plot, defined by eqn (10), was obtained by plotting q_e on the abscissa and q_e/C_e on the ordinate. The plot was used to calculate the number of binding sites from the x-intercept and the affinity constant between the adsorbate and the adsorbent (from the slope). A linear Scatchard's plot implies the presence of one type of binding site whereas a curvilinear plot indicates the presence of two or more binding sites.[22–24]

Hill's equation (eqn (11)) describes the binding of various species onto a homogeneous adsorbent. This model assumes that adsorption is a cooperative process in which adsorbates at one site of the adsorbent influence the other binding sites.[25,26]

$$\frac{q_e}{C_e} = K(B_{max} - q_e) \quad (10)$$

$$\log\left[\frac{v}{1-v}\right] = \log K + h \log C \quad (11)$$

where K is the association/affinity constant and equals the additive inverse of the slope, B_{max} is the maximum number of binding sites, v is the saturation fraction, equal to the amount of adsorbed BPB divided by the number of binding sites ($v = q/q_{max}$), C is the concentration of BPB, and h is the Hill's coefficient, which describes the cooperativity index.

Adsorption thermodynamics

The equilibrium constant (K) was determined from eqn (8) in thermodynamic experiments. The thermodynamic parameters (entropy (ΔS) and enthalpy (ΔH) changes) were calculated from the slope and the intercept of the plot of ln K *versus* $1/T$ using the van't Hoff equation (eqn (12)), and Gibb's free energy change (ΔG) was calculated from eqn (13) at different temperatures.[27,28]

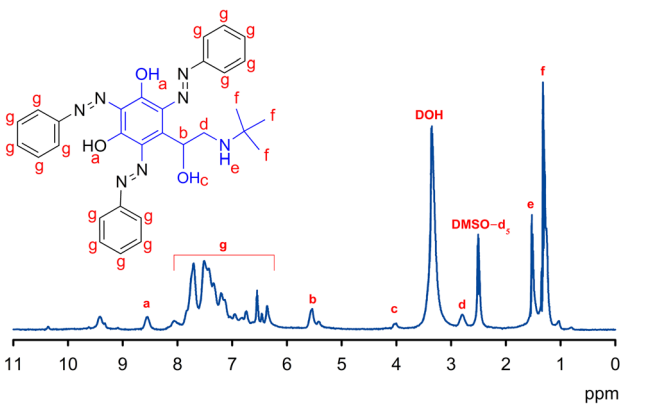

Fig. 3 ^{1}H-NMR spectrum of the synthesized AD using deuterated DMSO as a solvent and tetramethylsilane as an internal standard. The original NMR chart is depicted in Fig. S1 in the ESI.†

$$\ln K = -\frac{\Delta H}{RT} + \frac{\Delta S}{R} \quad (12)$$

$$\Delta G = \Delta H - T\Delta S \quad (13)$$

where K is the adsorption equilibrium constant (obtained from Freundlich's isotherm at different temperatures), ΔH is the enthalpy change (kJ mol^{-1}), ΔS is the entropy change (J mol^{-1} K^{-1}), R is the universal gas constant (8.314 J mol^{-1} K^{-1}), and T is the absolute adsorption temperature (K).

Results and discussion

Characterization of ADFS

The synthesized ADFS was characterized by Fourier transform infrared spectroscopy (FTIR), vibrating sample magnetometry (VSM), dynamic light scattering (DLS), X-ray diffractometry (XRD), scanning electron microscopy (SEM), ^{1}H-NMR spectroscopy, thermal analysis, and mass spectrometry.

FTIR spectroscopy. FTIR spectroscopy can be used for functional group analysis of the synthesized nanomaterials. The FTIR spectra of the plain SPIONs, AD, and ADFS were scanned over the spectral window 4000–400 cm^{-1}. The FTIR spectrum of the plain SPIONs clearly shows a distinct absorption band at 580 cm^{-1} representing the stretching vibration of Fe–O bond. The sharp absorption band observed at 1628 cm^{-1} may be attributed to the presence of carboxylic–metal (Fe–COO) linkage, so the surface of SPIONs must be negatively charged (see the zeta potential vlaues). A broad absorption band was detected at 3650–3000 cm^{-1}, which is attributed to the O–H stretching vibration in all of the depicted spectra.[11]

The FTIR spectrum of the synthesized AD is shown in Fig. 2A. The absorption bands observed at 3207 and 3065 cm^{-1} are assigned to the stretching vibrations of the N–H or O–H bonds. The absorption bands detected at 2980 and 2800 cm^{-1} correspond to the C–H stretching vibrations.[29,30] The bending of N–H was detected at 1593 cm^{-1}. Moreover, the absorption bands at 1477 and 1456 cm^{-1} are attributed to the bending of –C–H– bond. The absorption band at 1408 cm^{-1} is assigned to the stretching vibrations of N=N [169], [170]. In addition, the absorption bands appearing at 1297, 1207, 1122, and 1075 cm^{-1} stand for the C–N the stretching vibrations. Finally, the bands found in the region 650–1000 cm^{-1} correspond to –C=C– bending.[33–35]

Table 1 Assignment of the ^{1}H-NMR chemical shifts of the synthesized AD

Proton symbol (number)	Assignment	δ/ppm
a (2H)	Phenolic OH	8.5 (s)
b (1H)	CH	5.5 (t)
c (1H)	Aliphatic OH	4.0 (d)
d (2H)	CH_2	2.8 (d)
e (1H)	NH	1.5 (t)
f (9H)	CH_3	1.2 (s)
g (15H)	Aromatic CH	6.3–8.0 (m)

The FTIR spectrum of the synthesized ADFS (Fig. 2A) demonstrates a wide absorption band at 3155 cm^{-1} corresponding to the stretching vibrations of N–H and/or O–H, implying the existence of amino and hydroxyl groups that are able to form hydrogen bonds with the dissolved BPB ions. The band at 2908 cm^{-1} can be assigned to the C–H stretching vibration. Moreover, the absorption bands observed at 1965 and 1703 cm^{-1} may correspond to the stretching vibration of C=C. In addition, the absorption bands appearing at 1567 and 1408 cm^{-1} stand for N–H bond bending and the asymmetric vibration of –N=N–, respectively, thus confirming the formation of ADFS *via* the diazo coupling reaction. Furthermore, the stretching vibration of C–N was detected at 1274 and 1084 cm^{-1}. The sharp band at 560 cm^{-1} is attributed to the Fe–O stretching.[13,29–32,36]

XRD spectroscopy. XRD is a primary characterization technique used for the identification of crystalline materials, and it can provide information about the chemical composition and lattice parameters of the studied materials.[37] The XRD pattern of SPIONs (Fig. 2B) shows the characteristic peaks at 30.1, 35.5, 43.2, 53.5, 57.1, and 62.7° corresponding to the (220), (311), (400), (422), (511), and (440) diffraction planes of cubic crystalline Fe_3O_4. The above diffraction peaks coincide with those reported in the literature.[38]

^{1}HNMR spectroscopy. ^{1}H-NMR spectroscopy was used to elucidate the chemical structure of the synthesized AD. The ^{1}H-NMR spectrum of AD is depicted in Fig. 3, and the chemical shifts are tabulated in Table 1. A singlet peak was observed at 1.2 ppm, which can be attributed to the methyl protons (H_f) of TBDA. In addition, the triplet peak found at 1.5 ppm is characteristic for the proton of the secondary amino group (H_e). Moreover, a doublet peak was obtained at 2.8 ppm, which may be attributed to the aliphatic CH_2 protons (H_d). Furthermore, the aromatic protons of the aniline ring (H_g) could be seen as a multiplet peak at 6.3–8.0 ppm. Eventually, the singlet peak observed at 8.5 ppm might be attributed to the phenolic OH protons of TBDA (H_a).[39–42] However, the CH group (H_b) was observed as a triplet peak at 5.5 ppm. The two peaks observed at 2.5 and 3.3 ppm are due to the DMSO-d_5 and DOH resulting

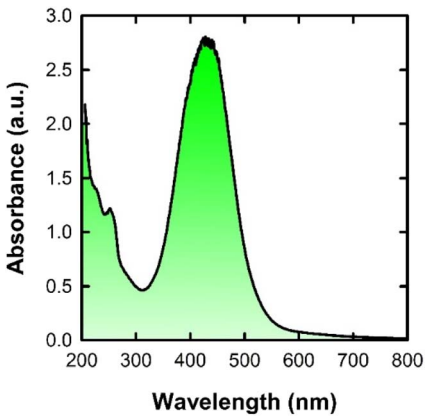

Fig. 4 UV-vis absorption spectrum of a 50 mg L^{-1} AD solution in absolute ethanol.

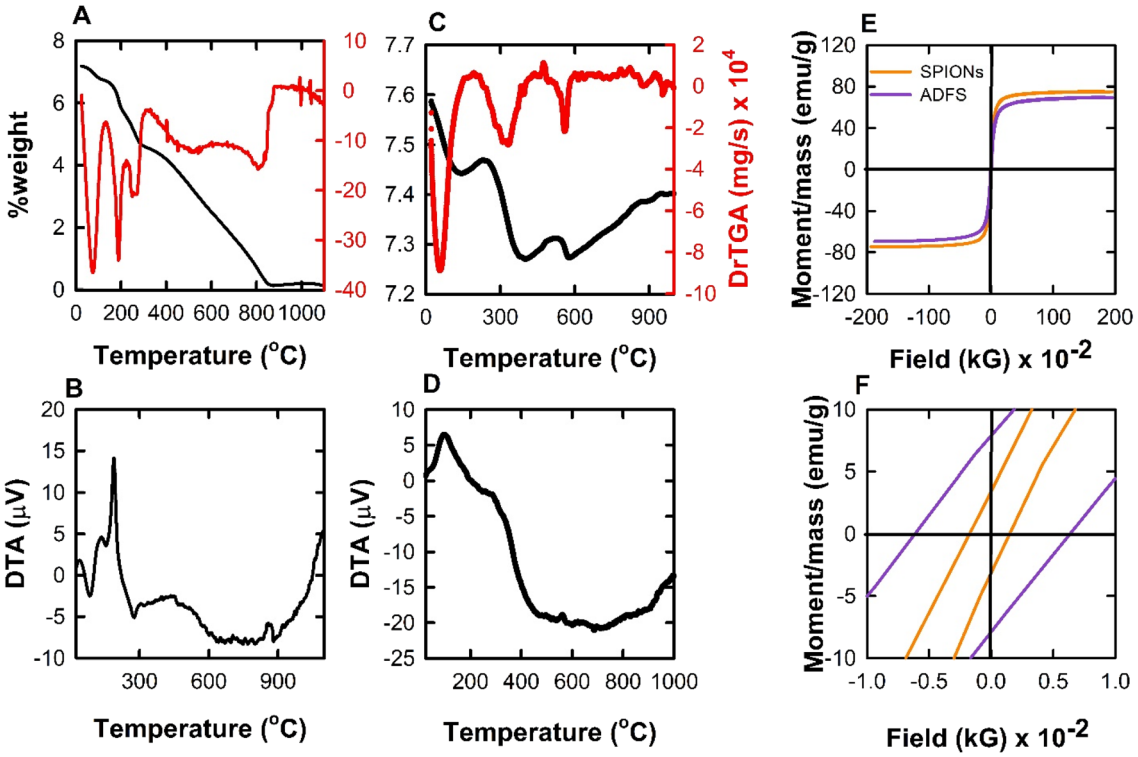

Fig. 5 (A and B) TGA and DTA thermograms of AD. (C and D) TGA and DTA thermograms of ADFS. (E and F) VSM plots of SPIONs and ADFS.

from the incomplete conversion of DMSO to DMSO-d_6, respectively.

UV-vis spectroscopy. Most organic compounds' electronic absorption spectra are in the visible and ultraviolet ranges. One or more electrons are promoted from the highest occupied molecular orbital, HOMO (or another lower energy occupied molecular orbital), to the lowest unoccupied molecular orbital, LUMO, during a transition of the molecule from a lower to a higher electronic state (or higher unoccupied orbitals). In the far ultraviolet range (λ < 200 nm), electronic transitions from bonding sigma orbitals (σ) to anti-bonding sigma orbitals (σ^*) are frequent. The n → π^* and π → π^* transitions, on the other hand, often take place at longer wavelengths, primarily in the near ultraviolet and visible ranges (200–400 nm). At wavelengths of 200 nm or longer, several transitions attributable to n → σ^* can be seen.[43] The UV-vis spectrum (200–800 nm) of AD in absolute ethanol demonstrates two distinct absorption bands (Fig. 4). The first absorption band appears at 255 nm and can be attributed to π → π^* transitions. However, the second absorption band which appears at 430 nm can be assigned to n → π^* electronic transition in the AD molecules.[44,45] The absorption of UV light is an evidence that the AD molecules are highly conjugated.

Thermal analysis. The thermal stability of the synthesized AD and ADFS was studied by using TGA and DTA in a nitrogen atmosphere at a heating rate of 10 °C per minute over a temperature range of 25–1100 °C. Fig. 5A and C show the TGA thermograms of the AD and ADFS, respectively. The TGA results revealed that the decomposition proceeds in five stages for the AD and two stages for the ADFS. In the case of the AD, the first thermal decomposition stage, which is accompanied by a weight loss of 5.76%, occurs in the temperature range of 25–112 °C, and this can be attributed to water evaporation. Upon raising the temperature above 300 °C, a sharp loss of sample mass is observed due to the degradation of the AD. The total weight loss of the AD with respect to the original sample weight was found to be 98.34%, which confirmed the complete degradation of the AD. The TGA thermogram of the ADFS (Fig. 5C) shows a slight weight loss of about 1.88% below 150 °C due to moisture. Above 200 °C, the weight loss is corresponding to the decomposition of the organic part of the ADFS sample (*i.e.*, the AD moiety). No further weight loss was observed above 457 °C, which indicates incomplete decomposition of the ADFS, thus confirming the presence of SPIONs in the sample.

The DTA curve of the AD (Fig. 5B) demonstrates endothermic and exothermic peaks during the thermal decomposition. The first endothermic peak can be observed at 84.74 °C and may be attributed to the loss of water molecules. The second exothermic peak was found at 188.60 °C and might be assigned to the oxidative decomposition of the AD. On the other hand, the DTA thermogram of the ADFS (Fig. 5D) shows one exothermic peak at 561 °C and one endothermic peak at 685.96 °C during the ADFS thermal decomposition. Thermal decomposition of TBDA may produce toxic gases such as carbon monoxide, carbon dioxide, and nitrogen oxides. The reaction that forms carbon monoxide or carbon dioxide is exothermic, which may account for the presence of the exothermic peak at 561 °C. However, the endothermic peak at 685.96 °C may be

attributed to bond cleavage during the thermal decomposition of the organic residues.[46]

Magnetic susceptibility. The magnetic properties of the plain SPIONs and the ADFS adsorbent were recorded under an external magnetic field between −20 and 20 kG at room temperature. The saturation magnetization (M_s) of the SPIONs and ADFS was found to increase sharply near the origin with negligible remnant magnetization (M_r) and coercivity values. Therefore, this suggests that the produced SPIONs and the ADFS have excellent paramagnetic properties (Fig. 5E and F). The reason behind the unique magnetic properties of the prepared SPIONs may be their tiny size.[47,48] The magnetization saturation of the adsorbent (69.47 emu g^{-1}) is higher than that of the SPIONs (74.92 emu g^{-1}), indicating that coating the SPIONs with the as-prepared AD did not affect their magnetic strength. Therefore, the obtained ADFS can be easily separated from the solution by an external magnetic field.

Mass spectrometry. The structure of the newly synthesized AD was elucidated with mass spectrometry. The molecular ion peak can be used to obtain the molecular mass of the synthesized AD, and can be considered a clue to confirm the successful synthesis of the designed chemical structure. The mass spectrum of the AD (Fig. S2†) shows a molecular ion peak at m/z 543, which agrees with the theoretically calculated molecular weight.

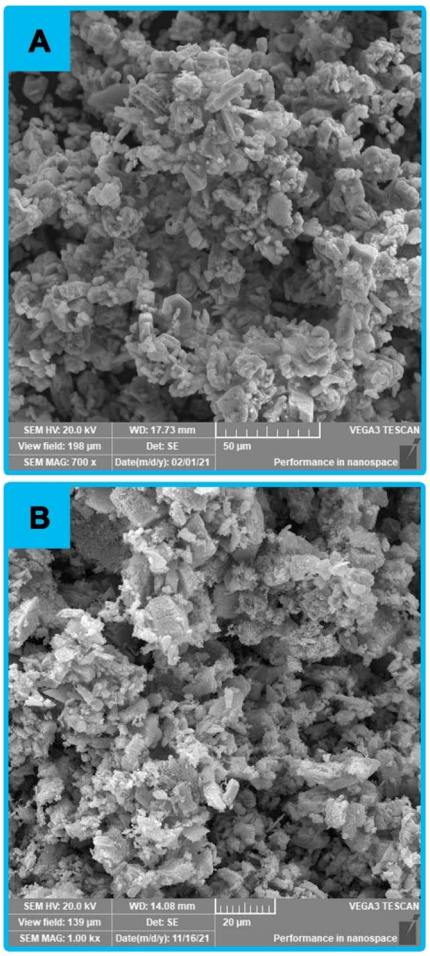

Fig. 6 Scanning electron micrographs of (A) plain SPIONs, and (B) ADFS.

Scanning electron microscopy. The surface morphology of the SPIONs and the ADFS was investigated by SEM imaging. The SEM images of bare/uncoated SPIONs (Fig. 6A) show cubic nanoparticles with smooth surfaces forming agglomerates that correspond to the typical structure of magnetite. Meanwhile, unlike bare SPIONs, the surface of the ADFS (Fig. 6B) is rough, implying the deposition of AD molecules onto the surface of the SPIONs.

Dynamic light scattering and zeta potential. The particle size distribution of the SPIONs and the ADFS was determined with the aid of DLS measurements in a water suspension. Prior to DLS measurement, the nanoparticle suspensions were sonicated for 15 min in an ultrasonic bath at room temperature to achieve good dispersion and distribution of the nanoparticles and to prevent particle agglomeration.[49] The average particle size of the SPIONs and the ADFS was about 46.1 and 176.5 nm, respectively. The increase in the size of the SPIONS is due to the formation of the ADFS on their surface *via* the diazo-coupling reaction.

Zeta potential measurements can be used as a measure of the stability of nanoparticles. The obtained negative ZP of the SPIONs (−23.4 mV) can be attributed to the presence of ionisable hydroxyl groups and carboxylate groups (mentioned above in the FTIR results). Upon coating the SPIONs with the AD, the negative ZP moved towards a more positive value (−14.2 mV) due to the cationic nature of the AD. These results confirm the successful formation of the magnetic ADFS adsorbent.[50,51]

It is obvious that coating SPIONs with AD resulted in a 4-folds increase in the average particle size in DLS measurement. This observation can be explained as follows. Coating of the SPIONs with an organic molecule may have led to a decrease in their inherent negative charge due to the presence of multiple organic functional groups as indicated by the more positive zeta potential values. Accordingly, the repulsion forces between the magnetite nanoparticles was decreased leading to easier agglomeration of the particles, thus giving a larger particle size in DLS measurements.

Adsorption of BPB by ADFS

Effect of solution pH. The solution pH plays a significant role in controlling the adsorption process. Both the degree of ionization of the BPB molecules and the surface charge of the ADFS can be significantly influenced by changes in solution pH due to possible protonation/deprotonation reactions. This leads to electrostatic attraction or repulsion between BPB molecules and the net surface charge on the ADFS adsorbent. The UV-vis absorption spectra of BPB dye in buffer solutions of various pH and the isosbestic point are shown in Fig. 7B.[52,53] The effect of pH on the adsorption of BPB from aqueous solutions by the ADFS is shown in Fig. 7C. In an acidic medium, BPB molecules are present in the lactoid ring structure, whereas in a basic medium the quinoid form is dominant (Fig. 7D).[54]

It was observed that the maximum adsorption efficiency of BPB was found to be 74.91% at a pH of 2. The adsorption

capacity and the removal percentage gradually decreased with increasing the pH of the solution, and the lowest BPB adsorption (6.76%) was recorded at pH 9. Therefore, the adsorption of BPB by the ADFS was favoured by lowering the pH; this can be attributed to the strong ionization of BPB ($pK_a = 4.3$).[55] At a solution pH < pK_a, neutral BPB molecules are present because of the protonation of the hydroxyl groups, leading to a corresponding increase in the electrostatic attraction between oxygen lone pairs of BPB and the positively charged ADFS surface due to the presence of protonated amino groups. In these conditions, the adsorption of BPB by ADFS is governed by non-covalent interactions such as hydrogen bonding and van der Waals forces. These findings coincide with the results of FTIR spectroscopy and the thermodynamic studies below. The adsorption efficiency was reduced at pH > pK_a due to the ionization of the BPB molecules, which hinders the adsorption process through electrostatic repulsion between the anionic form of BPB and the neutral surface of the ADFS (*i.e.*, due to the deprotonation of the ADFS amino groups). Consequently, the subsequent adsorption experiments were carried out at pH 2. Similar results were reported in the literature.[56]

Kinetics of BPB adsorption. Contact time between the adsorbent and the adsorbate in solution is a crucial parameter in the adsorption process, which should be studied because it allows for the adhesion of the BPB molecules onto the surface of the ADFS and it can reflect the kinetics of the adsorption process. The effect of contact time on the uptake efficiency of BPB by ADFS can be seen in Fig. 7E–G. The optimum contact time for adsorption is 120 min, where the removal efficiency was found to be 74.27% and the adsorption capacity is 7.43 mg g^{-1}. Initially, the rate of adsorption increased rapidly due to the presence of a large number of unoccupied active sites on ADFS. Furthermore, after contact for more than 120 min, the adsorption rate decreased because the binding active sites on the ADFS surface were saturated with the adsorbed BPB molecules, so that it could not bind to the adsorbent anymore and the adsorbed BBP molecules started to release back into the solution, leading to a corresponding decrease in the adsorption capacity and removal efficiency.[57]

The PFO kinetic model assumes that the rate of adsorbate uptake by the adsorbent is directly proportional to the difference in adsorbate concentration and the equilibrium saturation concentration of the adsorbate on the adsorbent.[58] The values of the equilibrium adsorption capacity, q_e, and the PFO constant, k_1, were determined from the slope and the intercept of a linear relation between $\log(q_e - q_t)$ and t. It was found that the adsorption of BPB onto the ADFS does not follow PFO kinetics because the calculated q_e value (0.08 mg g^{-1}) does not match the experimental value (7.43 mg g^{-1}) and due to the low correlation coefficient value ($r^2 = 0.3356$).

The PSO kinetic model has become the most popular model used to describe adsorption kinetics. The PSO model is based on the assumption that the adsorption rate depends on the number of available active sites on the ADFS surface and that chemisorption may be the rate-determining step. The second-order rate constant, k_2, and the equilibrium adsorption capacity, q_e, values could be calculated from the slope and the intercept of a plot between t/q_e against t, respectively (Fig. 7F). The high correlation coefficient ($r^2 = 0.9981$) and the close agreement between the calculated (7.12 mg g^{-1}) and experimental (7.43 mg g^{-1}) q_e values suggest that the adsorption of BPB onto the ADFS obeys the PSO kinetic model.[59,60]

The IPD kinetic model demonstrated three stages (Fig. 7G). The first stage (stage I) is due to exterior-surface adsorption or instantaneous adsorption, where the adsorption capacity increases rapidly due to the availability of more vacant active sites on the ADFS surface. The second stage (stage II) is attributed to gradual adsorption onto the interior surface of the ADFS. However, in the third stage (stage III), the adsorption reached equilibrium and then decreased due to the saturation of the binding active sites of the ADFS by the BPB molecules. Plotting q_e *versus* $t^{\frac{1}{2}}$ gives a linear relationship from which the IPD rate constant (k_{id}) and the constant I can be calculated from the slope and the intercept, respectively. The IPD rate constants (k_{id}) for stages I, II, and III are 0.25, 0.09, and −0.1 mg g^{-1} $min^{-1/2}$, respectively. It can be noticed that the adsorption rate constants are in the following order: stage I ($k_{id,1}$) > stage II ($k_{id,2}$) > stage III ($k_{id,3}$), thus confirming the above interpretation of the three stages of the IPD kinetic model. The deviation of the plot from the origin shows that IPD is not the only rate-limiting step. The I values are 5.52, 6.34, and 8.58 mg g^{-1} for stages I, II, and III, respectively, therefore indicating a large boundary layer effect.[61,62]

Effect of BPB concentration. The initial BPB concentration is a driving force to overcome the mass transfer resistance of BPB molecules between the ADFS surface and the bulk solution.[63] Fig. 8A shows the effect of changing the initial concentration of BPB on the adsorption capacity and the efficiency of BPB removal by the ADFS. As can be seen from Fig. 8A, the BPB removal efficiency decreases from 80.45 to 49.59%, and the equilibrium adsorption capacity increases from 4.02 to 24.80 mg g^{-1} when the BPB initial concentration increases from 10 to 100 mg L^{-1}. At low initial BPB concentrations, a large number of vacant/unoccupied active binding sites on the ADFS surface are present, which explains the high adsorption efficiency values. When the initial BPB concentration increases at a fixed ADFS dose, the number of BPB adsorption sites becomes insufficient to accommodate the high concentration of BPB present in the solution (due to the saturation of the adsorption sites by the BPB molecules), which eventually leads to a decrease in the adsorption efficiency/removal percentage.[64]

The adsorption isotherms were used to describe the relationship between the adsorption capacity of BPB (q_e) and the remaining concentration of BPB at equilibrium (C_e). The adsorption data obtained from the variation of BPB concentration was analysed using the Langmuir, Freundlich, and Temkin isotherms in order to investigate the adsorption behaviour of BPB onto the ADFS surface.[65] In the present study, the r^2 values were 0.9968, 0.9524, and 0.9428 for the Freundlich, Langmuir, and Temkin isotherms, respectively. Therefore, the adsorption of BPB molecules onto the ADFS follows the Freundlich isotherm model, which demonstrated the highest r^2 value (Fig. 8B). This result implies that the adsorption of BPB by the ADFS is a heterogeneous multilayer adsorption.

The Freundlich constant (n) can help in investigating the mechanism of the adsorption process and indicate whether it is

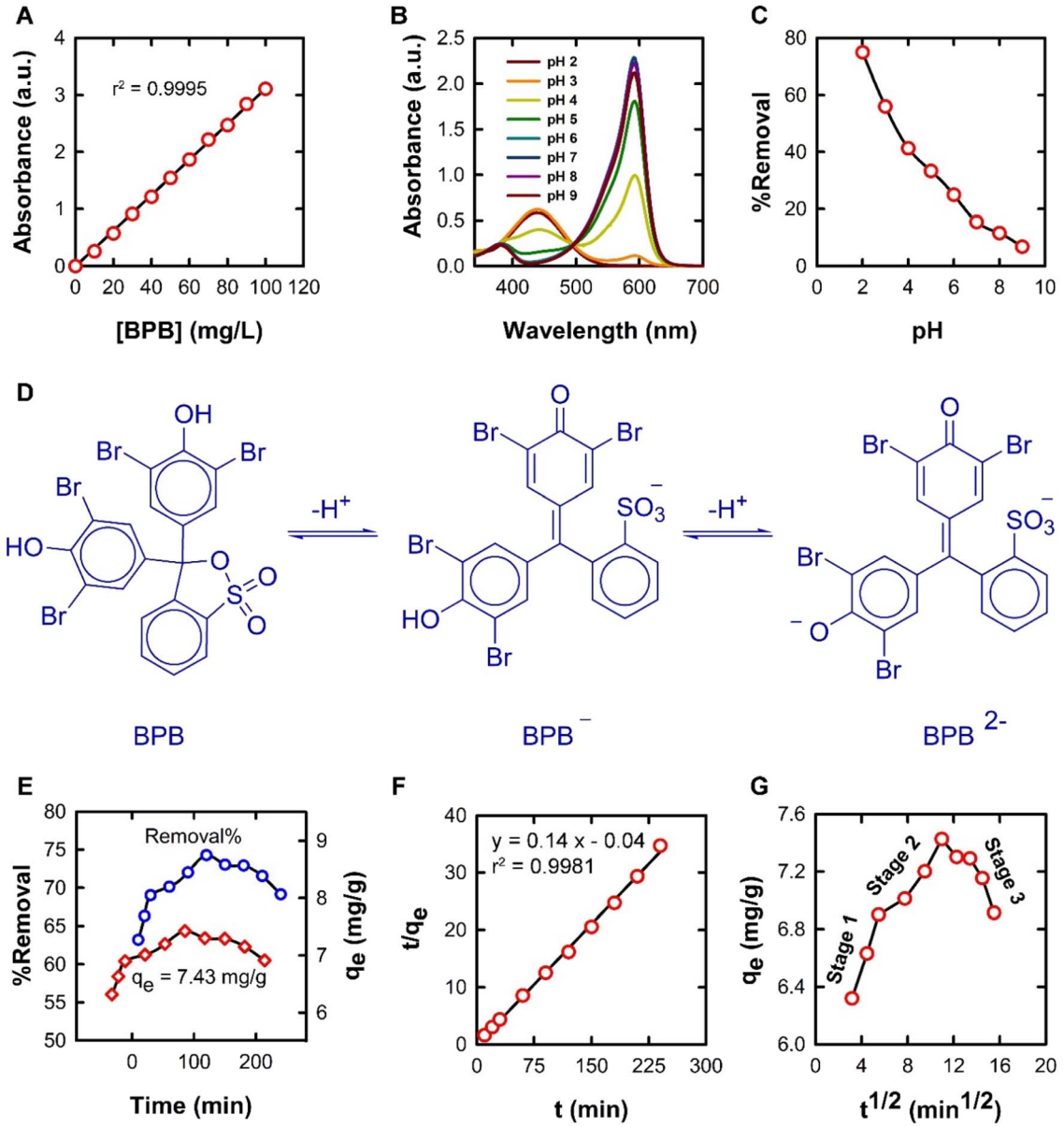

Fig. 7 (A) Standard plot for the spectrophotometric determination of BPB concentrations from 10 to 100 mg L^{-1} at 436 nm; (B) UV-vis absorption spectra of aqueous BPB solutions of different pH values showing the isosbestic point; (C) effect of changes in pH on the removal of BPB by the proposed ADFS adsorbent; (D) equilibrium protonation/deprotonation reactions of BPB in aqueous media; (E) effect of changing contact time on the removal of BPB; (F) PSO kinetic model; and (G) the IPD model for the adsorption of BPB onto the ADFS. The raw data of the IPD model is summarised in Table S1 in the ESI.†

a difficult/unfavourable chemisorption process (where $n < 1$), a linear process (where $n = 1$) or a favourable physisorption process (where $n > 1$). The Freundlich constants n and K_F values were found to be 1.82 and 11.50, respectively, indicating that the adsorption of BPB by the ADFS surface is favourable and occurs through a physisorption mechanism. Basically, physisorption processes take place due to weak intermolecular forces such as van der Waals forces between the adsorbate molecules (*i.e.*, BPB) and the adsorbent (*i.e.*, ADFS) surface.[11,66,67]

From the Langmuir plot (Fig. 8C), the calculated values of q_{max} and b were found to be 32.57 mg g^{-1} and 0.05, respectively. The essential characteristics of the Langmuir isotherm model can be expressed in terms of the separation factor (R_L), which can be explained by eqn (14). The value of R_L describes the mechanism of the adsorption process, which might be unfavourable ($R_L > 1$), linear ($R_L = 1$), favourable ($0 < R_L < 1$), or irreversible ($R_L = 0$). Herein, the obtained R_L value is 0.05, thus confirming that the adsorption of BPB onto the ADFS surface is favourable.[68]

$$R_L = \frac{1}{1 + bC_o} \quad (14)$$

where b is the Langmuir's constant in mg g^{-1}, and C_o is the initial BPB concentration in mg L^{-1}.

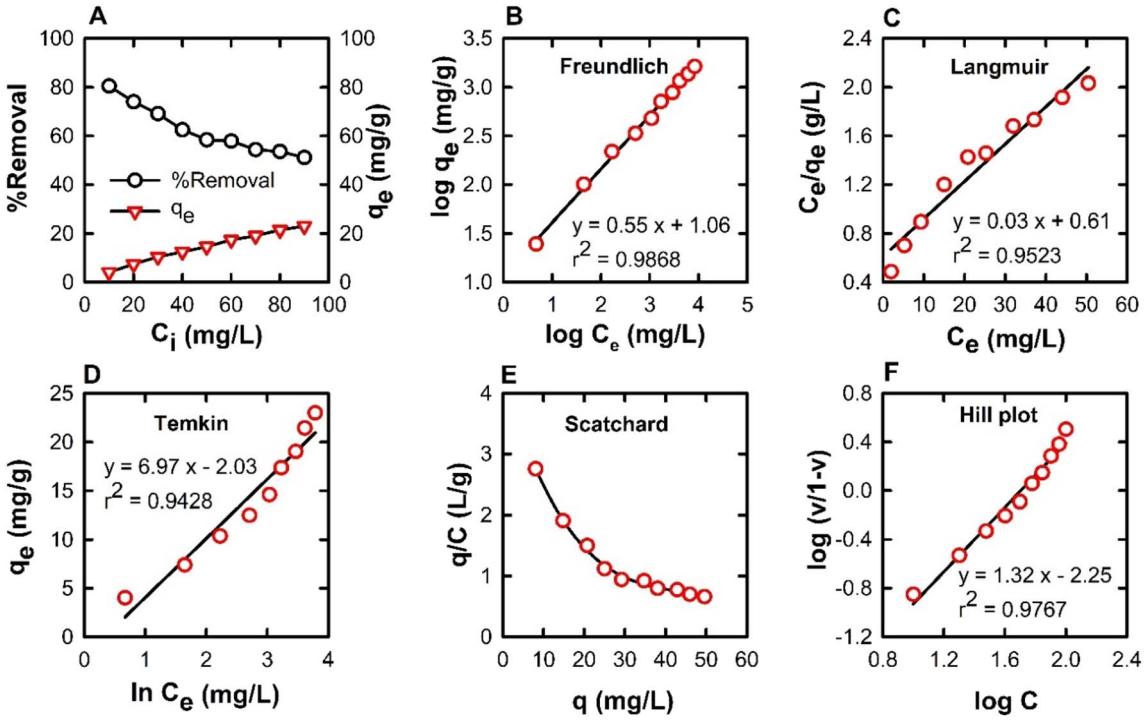

Fig. 8 (A) Effect of BPB on the percent removal and equilibrium adsorption capacity of the ADFS, (B) Freundlich isotherm, (C) Langmuir isotherm, (D) Temkin isotherm, (E) Scatchard plot, and (F) Hill plot for the adsorption of BPB molecules onto the ADFS adsorbent.

The Temkin isotherm model is based on the assumption that the heat of adsorption of all molecules in the layer decreases linearly with the increase in the adsorbent surface coverage. The Temkin constants, b_T and A_T, are derived from the slope and the intercept of a graph of $\ln C_e$ against q_e, respectively (Fig. 8D). The value of b_T can be used for the prediction of the type of adsorption; b_T values $< 8 \times 10^4$ are usually ascribed to physisorption processes. The values of $B = RT/b_T$ and b_T are 6.07 (lower than 8 kJ mol^{-1}) and 408.27, respectively, meaning that the adsorption of BPB onto the ADFS is governed by a physisorption process where a weak interaction occurs between the adsorbate molecules and the adsorbent surface.[69,70]

The specific binding data was analysed using the Scatchard and Hill plots to estimate the binding parameters such as the affinity/association constant (K), the maximum number of binding sites (B_{max}), the cooperativity index (h), and to understand the interaction of the adsorbent with the adsorbate.

According to calculations carried out in Scatchard analysis, the B_{max} and K values are 58.62 and 0.04 g L^{-1}, respectively. In the Scatchard plot analysis (Fig. 8E), the concave upward curve is indicative of the presence of multiple binding sites or nonspecific binding sites on the ADFS surface.[71,72] Moreover, the non-linear Scatchard plot can be approximately divided into two linear segments corresponding to low and high concentration intervals of BPB. The large value of K in the low concentration interval can be attributed to the presence of a large number of vacant BPB-binding sites on the ADFS surface, which leads to a high adsorption efficiency. However, at high concentrations of BPB, the adsorption efficiency decreases with increasing the concentration, which may be attributed to the saturation of the adsorption sites with the BPB molecules, as indicated by the low K value. According to the calculations of Scatchard plot, in the low concentration interval of Scatchard plots (10–50 mg L^{-1}), the B_{max} and K values were found to be 38.77 and 0.08 g L^{-1}, respectively. However, in the high concentration interval (60–100 mg L^{-1}), the B_{max} and K values were found to be 90.94 and 0.01 g L^{-1}, respectively.

The calculated Hill coefficient (a.k.a. the cooperativity index) (h) from the plot in Fig. 8F is 1.32 (*i.e.*, greater than 1) indicating the presence of at least two different types of binding sites on the ADFS with positive cooperativity. The findings mentioned above about Scatchard analysis, which demonstrated a concave-upward curve, agree with the results obtained from the Hill plot, and both of them indicate the presence of multiple classes of binding sites.[73,74]

Amount of ADFS. The amount of the adsorbent (a.k.a. adsorbent dose) plays an important role in controlling the rate of adsorption because it determines the adsorbent capacity for a given initial concentration of the adsorbate.[75] The effect of the ADFS dose on the adsorption of BPB was investigated by increasing the mass of the adsorbent from 20 to 250 mg, and the results are illustrated in Fig. 9A. It was observed that the removal efficiency increased from 74.91 to 98.52 when the

Table 2 Thermodynamic parameters for BPB adsorption onto the proposed ADFS adsorbent

ΔH (kJ mol^{-1})	ΔS (kJ mol^{-1} K^{-1})	ΔG (kJ mol^{-1})			
		303 K	313 K	323 K	333 K
−82.19	−0.24	−8.03	−5.24	−3.12	−0.58

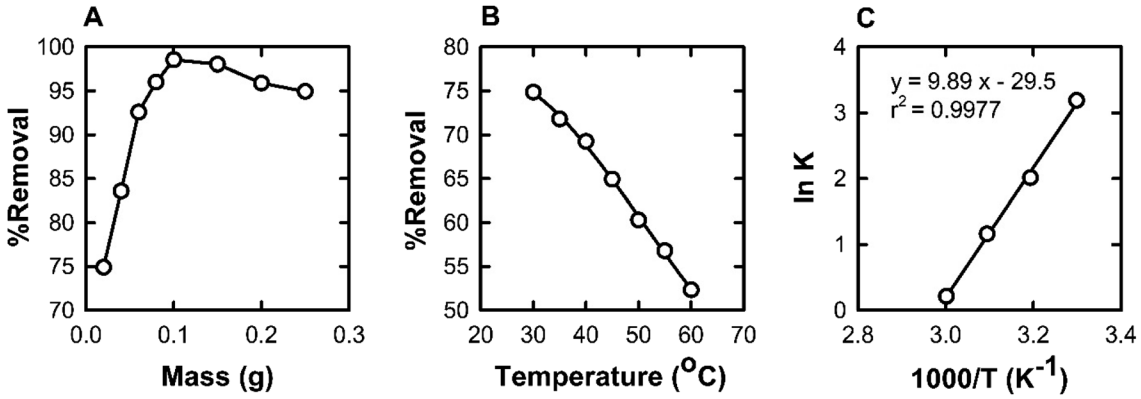

Fig. 9 Effect of changing the mass of the ADFS (A), and the test solution temperature (B) on the percent removal of BPB, and the plot between ln *K* and 1000/*T* used to calculate the thermodynamic parameters of the adsorption process (C).

amount of ADFS was increased from 20 to 100 mg. This observation might be attributed to the addition of a new number of available binding sites in solution.[76] However, the removal efficiency decreased from 98.52 to 94.93% upon increasing the ADFS dose from 100 to 250 mg. This observation is due to the saturation of the adsorbent sites and reaching of equilibrium.[77] This can be attributed to the aggregation of the adsorbent upon increasing the ADFS dose, resulting in a corresponding decrease in the available adsorbent surface area for adsorbate, and an increase in the diffusion path length; thus lowering the removal efficiency.[78]

BPB adsorption thermodynamics. The influence of changing the test solution temperature on the adsorption of BPB molecules onto the proposed ADFS is presented in Fig. 9B. The adsorption efficiency demonstrated a noticeable decrease as the test solution temperature was increased from 303 to 333 K. Therefore, the adsorbed BPB molecules on the ADFS surface showed a tendency to desorb from their binding sites at elevated temperatures. The obtained results demonstrated that the synthesized ADFS is a promising low-cost candidate adsorbent for the highly efficient removal of BPB from contaminated water because it shows the best behaviour at room temperature. The values of the thermodynamic parameters (ΔH, ΔS, and ΔG) that control the spontaneity of the adsorption process are collected in Table 2.

Generally, ΔG values for chemisorption processes range from -400 to -80 kJ mol^{-1}, while those of physisorption processes are between -20 and 0 kJ mol^{-1}. The calculated ΔG was found to be between -0.59 and -8.03 kJ mol^{-1}, which indicates that the adsorption of BPB is a spontaneous physisorption process. These results coincide with the results discussed in Section 3.2.3.[79,80]

The most common four types of noncovalent interactions are van der Waals forces, electrostatic interactions, hydrogen bonding, and hydrophobic effects. The hydrophobic interaction can be either an entropy-driven process ($\Delta S > 0$, $\Delta H > 0$ and $|\Delta H| < |T\Delta S|$) or an enthalpy-driven process such as van der Waals interactions and hydrogen bonding ($\Delta S < 0$, $\Delta H < 0$ and $|\Delta H| > |T\Delta S|$). However, electrostatic interactions are characterized by a positive ΔS value and a minor value of ΔH ($\Delta S > 0$, $\Delta H \sim 0$ or $\Delta H > 0$).[81,82] The negative values of ΔH and ΔS (Table 2) imply that the adsorption of BPB on the proposed ADFS adsorbent is an exothermic process and takes place *via* van der Waals interactions and/or hydrogen bonding between the adsorbent and the adsorbate molecules.[83] Table 3 summarises the obtained adsorption parameters in the present study along with some of the parameters reported in the literature.

Table 3 Comparison between the adsorption parameters of the present study and those in the literature

Adsorbent	q_{max} (mg g^{-1})	Kinetics	Isotherms	References
ADFS	7.43	PSO	Freundlich	This work
Polyacrylonitrile (PAN) nanofiber	0.89	PSO	Freundlich	84
ZnO NPs	3.10	PSO	Freundlich	85
Musa acuminata peel	6.04	PFO	Freundlich	86
Labeo bata fish scale	7.39	PSO/IPD	Freundlich	87
AgNP impregnation of pristine *Solanum tuberosum* peel	9.60	PFO/IPD	Freundlich	88
Polymer-clay composite	10.7	PFO	Freundlich	89
Polyethyleneimine-coated SPIONs	11.3	PSO	Freundlich	90
CuO NPs	20.2	PFO	Langmuir	91
α-Chitin nanoparticles	22.7	PSO	Langmuir	7
Graphene oxide nanoparticles	28.6	—	Langmuir	92
Fe_3O_4–CuO-AC composite	88.6	PSO	—	93
Co, Mn, and Fe-modified graphene oxide	94.3	PSO	Langmuir	94

Conclusions

In the current study, a novel magnetic adsorbent with an azo dye functionalization has been prepared to remove the anionic dye bromophenol blue from contaminated water. The proposed adsorbent is synthesized from biocompatible super-paramagnetic iron oxide nanoparticles, which are the end product of a diazo-coupling reaction between aniline and a common substance used in pharmaceutical industries (TBDA). The proposed adsorbent may be easily separated from water by applying a strong external magnetic field. Hence, BPB and other anionic contaminants might be removed successfully from water using the proposed adsorbent nanomaterial. The recommended ADFS's synthesis protocol is simple, repeatable, scalable, and quick. A continuation of this work is required to investigate other new azo dyes so as to come up with novel magnetic adsorbents with better adsorption capacities and broader applications.

Author contributions

Hadeel Saad: methodology, investigation, formal analysis, visualization, data curation, resources, writing – original draft. F. A. Nour El-Dien: supervision, project administration, resources, writing – review and editing. Nadia E. A. El-Gamel: supervision, writing – review and editing. Ahmed S. Abo Dena: conceptualization, methodology, investigation, resources, formal analysis, data curation, visualization, writing – review and editing, supervision, project administration.

Conflicts of interest

There are no conflicts to declare.

Notes and references

1 Y. Zhang, X. Hong, X.-M. Cao, X.-Q. Huang, B. Hu, S.-Y. Ding and H. Lin, *ACS Appl. Mater. Interfaces*, 2021, **13**, 6359–6366.
2 A. E. Segneanu, C. Orbeci, C. Lazau, P. Sfirloaga, P. Vlazan, C. Bandas and I. Grozescu, in *Water Treatment*, ed. W. Elshorbagy and R. K. Chowdhury, IntechOpen, Rijeka, 2013, ch. 4, pp. 53–80.
3 T. Shah, T. Gul and K. Saeed, *Appl. Water Sci.*, 2019, **9**, 105.
4 A. Azanaw, B. Birlie, B. Teshome and M. Jemberie, *Case Stud. Chem. Environ. Eng.*, 2022, **6**, 100230.
5 P. R. de Souza, T. M. do Carmo Ribeiro, A. P. Lôbo, M. S. Tokumoto, R. M. de Jesus and I. P. Lôbo, *Environ. Monit. Assess.*, 2020, **192**, 197.
6 M. Essandoh and R. A. Garcia, *Chemosphere*, 2018, **206**, 502–512.
7 S. Dhananasekaran, R. Palanivel and S. Pappu, *J. Adv. Res.*, 2016, **7**, 113–124.
8 Z. Chen, X. Song, W. W. M. Soh, Y. Wen, J. Zhu, M. Zhang and J. Li, *Gels*, 2021, **7**(4), 1–13.
9 P. Chauhan, K. K. Bhasin and S. Chaudhary, *Environ. Sci. Pollut. Res. Int.*, 2021, **28**, 61344–61359.
10 A. S. Shair, A. S. Abo Dena and I. M. El-Sherbiny, *Spectrochim. Acta, Part A*, 2021, **249**, 119301.
11 H. Saad, F. A. Nour El-Dien, N. E. A. El-Gamel and A. S. Abo Dena, *RSC Adv.*, 2021, **11**, 39768–39780.
12 S. S. Laha, N. D. Thorat, G. Singh, C. I. Sathish, J. Yi, A. Dixit and A. Vinu, *Small*, 2021, 2104855.
13 Y. Shen, W.-X. Ni and B. Li, *ACS Omega*, 2021, **6**, 3202–3208.
14 S. Moosavi, C. W. Lai, S. Gan, G. Zamiri, O. Akbarzadeh Pivehzhani and M. R. Johan, *ACS Omega*, 2020, **5**, 20684–20697.
15 A. Muthu Kumara Pandian, M. Rajasimman, N. Rajamohan, S. Varjani and C. Karthikeyan, *J. Hazard. Mater.*, 2021, **416**, 125717.
16 G. Shah, M. Imran, U. Aiman, M. Iqbal, M. Akram, H. M. R. Javeed, A. Waqar and F. Rabbani, *PeerJ Phys. Chem.*, 2022, **4**, e21.
17 M. Pourshaban, E. Moniri, R. Safaeijavan and H. A. Panahi, *Korean Chem. Eng. Res.*, 2021, **59**, 493–502.
18 R. Prasad, D. Sharma, K. Yadav and H. Ibrahim, *Can. J. Chem. Eng.*, 2021, **100**, 439–450.
19 S. A. Al-Trawneh, A. G. Jiries, S. F. Alshahateet and S. Sagadevan, *Chem. Phys. Lett.*, 2021, **781**, 138959.
20 N. Ayawei, A. N. Ebelegi and D. Wankasi, *J. Chem.*, 2017, **2017**, 3039817.
21 M. Erhayem, F. Al-Tohami, R. Gaith and K. Ahmida, *Am. J. Anal. Chem.*, 2015, **06**, 1–10.
22 R. Brion-Roby, J. Gagnon, J.-S. Deschênes and B. Chabot, *Pure Appl. Chem.*, 2018, **90**, 63–77.
23 Y. Cui, L. Jiang, H. Li, D. Meng, Y. Chen, L. Ding and Y. Xu, *J. Ind. Eng. Chem.*, 2021, **96**, 382–389.
24 M. Mabrouk, S. F. Hammad, A. A. Abdella and F. R. Mansour, *Int. J. Biol. Macromol.*, 2022, **200**, 327–334.
25 H. Ramezanipour Penchah, P. Najafi, A. Ghaemi and H. Ghanadzadeh Gilani, *Environ. Prog. Sustainable Energy*, 2021, **40**, e13586.
26 C. Rodwihok, M. Suwannakeaw, K. Charoensri, D. Wongratanaphisan, S. Woon Woo and H. S. Kim, *Bioresour. Technol.*, 2021, **331**, 125060.
27 K. Kayalvizhi, N. M. I. Alhaji, D. Saravanakkumar, S. B. Mohamed, K. Kaviyarasu, A. Ayeshamariam, A. M. Al-Mohaimeed, M. R. AbdelGawwad and M. S. Elshikh, *Environ. Res.*, 2022, **203**, 111814.
28 I. Raya, G. Widjaja, Z. H. Mahmood, A. J. Kadhim, K. O. Vladimirovich, Y. F. Mustafa, M. M. Kadhim, T. Mahmudiono, I. Husein and L. Kafi-Ahmadi, *Appl. Phys. A*, 2022, **128**, 167.
29 Y. Wang, Z. Xie, X. Wang, X. Peng and J. Zheng, *J. Nanobiotechnol.*, 2021, **19**, 260.
30 Q. A. Alsulami, H. S. Alorfi and S. M. A. S. Keshk, *Polym.-Plast. Technol. Mater.*, 2022, 1–9.
31 W. Wen-Qiong, Z. Jie-Long, Y. Qian, Z. Ji-Yang, L. Mao-Lin, G. Rui-Xia and H. Yujun, *RSC Adv.*, 2021, **11**, 26291–26302.
32 D. Liu, J. Yuan, J. Li and G. Zhang, *ACS Omega*, 2019, **4**, 12680–12686.
33 S. M. El-Megharbel, R. Z. Hamza, A. A. Gobouri and M. S. Refat, *Appl. Organomet. Chem.*, 2019, **33**, e4892.

34 R. Samantha and D. Almalik, *Bull. Chem. Soc. Ethiop.*, 2021, **35**, 601–614.
35 R. Roy and S. Prasad, *IOP Conf. Ser.: Mater. Sci. Eng.*, 2021, **1120**, 012028.
36 S. M. El-Megharbel, R. Z. Hamza, A. A. Gobouri and M. S. Refat, *Appl. Organomet. Chem.*, 2019, **33**, 1–15.
37 Y. Pu, Y. Niu, Y. Wang, S. Liu and B. Zhang, *Particuology*, 2022, **61**, 11–17.
38 M. Khalkhali, K. Rostamizadeh, S. S. Sadighian, F. Khoeini, M. Naghibi and M. Hamidi, *Daru J. Pharm. Sci.*, 2015, **23**(45), 1–12.
39 S. Mandal and V. Gonela, *Dalton Trans.*, 2016, **45**, 7421–7426.
40 R. K. Harris, P. Hodgkinson, V. Zorin, J.-N. Dumez, B. Elena-Herrmann, L. Emsley, E. Salager and R. S. Stein, *Magn. Reson. Chem.*, 2010, **48**, S103–S112.
41 E. Varga, G. Benkovics, A. Darcsi, B. Várnai, T. Sohajda, M. Malanga and S. Béni, *Electrophoresis*, 2019, **40**, 2789–2798.
42 M. S. Refat and M. El-Megharbel Samy, *Spectrosc. Spectral Anal.*, 2021, **41**, 3316–3320.
43 A. S. Abo Dena and S. A. Abdel Gaber, *Spectrochim. Acta, Part A*, 2017, **181**, 239–248.
44 R. K. Karthick, J. Kavitha and K. S. Lakshmi, *Res. J. Pharm. Technol.*, 2020, **13**, 767–773.
45 S. Gul, A. U. H. A. Shah and S. Bilal, *J. Phys.: Conf. Ser.*, 2013, **439**, 1–10.
46 R. García-Muelas, Q. Li and N. López, *ACS Catal.*, 2015, **5**, 1027–1036.
47 A. V. Samrot, H. H. Ali, J. A. Selvarani, E. Faradjeva, P. Raji, P. Prakash and S. S. Kumar, *Curr. Res. Green Sustainable Chem.*, 2021, **4**, 100066.
48 A. Farhana, A. Jenifer Selvarani, A. V Samrot, A. Alsrhani, P. Raji, C. S. Sahithya, P. J. Jane Cypriyana, P. Senthilkumar, M. P. Ling and S. Yishak, *J. Nanomater.*, 2022, **2022**, 4326939.
49 J. Shah, M. Ranjan, P. Thareja and P. Estellé, *J. Therm. Anal. Calorim.*, 2022, **147**, 10319–10328.
50 W. M. Ng and J. K. Lim, *Colloid Interface Sci. Commun.*, 2022, **46**, 100582.
51 S. Mohapatra, M. Asfer, M. Anwar, K. Sharma, M. Akhter, F. J. Ahmad and A. A. Siddiqui, *Heliyon*, 2019, **5**, e01955.
52 S. Banerjee and M. C. Chattopadhyaya, *Arabian J. Chem.*, 2017, **10**, S1629–S1638.
53 L. Anah and N. Astrini, *IOP Conf. Ser.: Earth Environ. Sci.*, 2017, **60**, 12010.
54 D. Goncalves, *Open Chem.*, 2016, **14**, 404–411.
55 A. Shokrollahi and E. Zare, *J. Mol. Liq.*, 2016, **219**, 1165–1171.
56 E. Rápó, R. Szép, Á. Keresztesi, M. Suciu and S. Tonk, *Acta Chim. Slov.*, 2018, **65**, 709–717.
57 D. Kurniawati, B. Bahrizal, T. K. Sari, F. Adella and S. Sy, *J. Phys.: Conf. Ser.*, 2021, **1788**, 012008.
58 E. Nyankson, J. Adjasoo, J. K. Efavi, A. Yaya, G. Manu, A. Kingsford and R. Y. Abrokwah, *Sci. Afr.*, 2020, **7**, e00257.
59 G. William Kajjumba, S. Emik, A. Öngen, H. Kurtulus Özcan and S. Aydın, *Adv. Sorption Process Appl.*, 2019, 1–19.
60 S. Ebrahimpoor, V. Kiarostami, M. Khosravi, M. Davallo and A. Ghaedi, *Fibers Polym.*, 2021, **22**, 159–170.
61 C. Xiong, S. Wang, L. Zhang, Y. Li, Y. Zhou and J. Peng, *Polymers*, 2018, **10**(2), 159–174.
62 S. D. Mekkey, *Curr. Sci. Int.*, 2017, **6**, 58–74.
63 S. Shamim, in *Biosorption*, ed. J. Derco and B. Vrana, IntechOpen, Rijeka, 2018.
64 R. Beksissa, B. Tekola, T. Ayala and B. Dame, *Environ. Challenges*, 2021, **4**, 100091.
65 I.-H. T. Kuete, D. R. T. Tchuifon, G. N. Ndifor-Angwafor, A. T. Kamdem and S. G. Anagho, *J. Encapsulation Adsorpt. Sci.*, 2020, **10**, 1–27.
66 A. Bouzidi, M. Djedid, C. Ad, M. Benalia, B. Hafez and H. Elmsellem, *Moroccan J. Chem.*, 2021, **9**, 156–167.
67 T. Tatarchuk, A. Shyichuk, Z. Sojka, J. Gryboś, M. Naushad, V. Kotsyubynsky, M. Kowalska, S. Kwiatkowska-Marks and N. Danyliuk, *J. Mol. Liq.*, 2021, **15**, 115375.
68 H. S. Y. Akrawi, M. A. Al-Obaidi and C. H. Abdulrahman, *IOP Conf. Ser.: Earth Environ. Sci.*, 2021, **761**, 012017.
69 R. Ragadhita and A. B. D. Nandiyanto, *J. Eng. Sci. Technol.*, 2022, **17**, 1078–1089.
70 T. Z. E. Lee, J. Zhang, Y. Feng, X. Lin and J. Zhou, *IOP Conf. Ser.: Earth Environ. Sci.*, 2021, **657**, 12026.
71 V. Casadó-Anguera and V. Casadó, *Expert Opin. Drug Discovery*, 2022, 1–27.
72 N. T. Abdel, H. Abdulla, M. S. Rizk and A. S. Abo, *Sens. Actuators, B*, 2019, **283**, 6–17.
73 J. L. Alesio, A. Slitt and G. D. Bothun, *Chemosphere*, 2022, **287**, 131979.
74 T.-T. T. Nguyen, S. Ramachandran, M. J. Hill and R. A. Cerione, *J. Biol. Chem.*, 2022, **298**(2), 101564.
75 E. Vunain, D. Kenneth and T. Biswick, *Appl. Water Sci.*, 2017, **7**, 4301–4319.
76 J. Meng, X. Lin, H. Li, Y. Zhang, J. Zhou, Y. Chen, R. Shang and X. Luo, *RSC Adv.*, 2019, **9**, 8091–8103.
77 N. Turki, N. Boujelben, Z. Bakari and J. Bouzid, *Am. J. Environ. Sci.*, 2021, **17**, 92–100.
78 H. M. El Refay, A. M. Raslan and A. M. E. Atia, *Egypt. J. Chem.*, 2022, **65**, 977–991.
79 A. K. Sakr, M. F. Cheira, M. A. Hassanin, H. I. Mira, S. A. Mohamed, M. U. Khandaker, H. Osman, E. M. Eed, M. I. Sayyed and M. Y. Hanfi, *Appl. Sci.*, 2021, **11**, 10320.
80 A. Swelam, A. Salem, A. Aanym and A. Farghly, *Al-Azhar Bull. Sci.*, 2018, **29**(1), 45–58.
81 T. A. Wani, A. H. Bakheit, M. A. Abounassif and S. Zargar, *Front. Chem.*, 2018, **6**(47), 1–9.
82 C. Wu, X. Lou, X. Xu, A. Huang, M. Zhang and L. Ma, *ACS Omega*, 2020, **5**, 4191–4199.
83 A. N. Ebelegi, N. Ayawei and D. Wankasi, *Open J. Phys. Chem.*, 2020, **10**, 166–182.
84 M. B. Chabalala, M. Z. Al-Abri, B. B. Mamba and E. N. Nxumalo, *Chem. Eng. Res. Des.*, 2021, **169**, 19–32.
85 K. G. Akpomie, S. Ghosh, M. Gryzenhout and J. Conradie, *Sci. Rep.*, 2021, **11**, 8305.
86 K. G. Akpomie and J. Conradie, *Arabian J. Chem.*, 2020, **13**, 7115–7131.
87 A. Ghosh, H. S. Biswas, S. Debnath, P. Sasikumar, K. Biswas and U. C. Ghosh, *Indian J. Chem. Technol.*, 2019, **26**, 321–329.
88 K. G. Akpomie and J. Conradie, *Sci. Rep.*, 2020, **10**, 17094.

89 A. A. El-Zahhar, N. S. Awwad and E. E. El-Katori, *J. Mol. Liq.*, 2014, **199**, 454–461.
90 A. S. Shair, A. S. A. Dena and I. M. El-Sherbiny, *Spectrochim. Acta, Part A*, 2021, **249**, 119301.
91 M. Rashad and H. A. Al-Aoh, *Desalin. Water Treat.*, 2019, **139**, 360–368.
92 S. Zahran, S. Makharza, M. Atawneh, F. Takrori, I. Bsileh, S. Hampel and B. Büchner, *Adv. Mater. Process. Technol.*, 2022, **8**, 4280–4296.
93 A. Q. Alorabi, M. Shamshi Hassan and M. Azizi, *Arabian J. Chem.*, 2020, **13**, 8080–8091.
94 H. Örtün and N. Karapınar, *Russ. J. Phys. Chem. A*, 2021, **95**, S179–S188.